J Electroceram (2015) 34:82–90
DOI 10.1007/s10832-014-9946-9

Study of compaction and sintering of nanosized oxide powders by in situ electrical measurements and dilatometry: Nano CeO_2—case study

P. Knauth · J. Engel · S. R. Bishop · H. L. Tuller

Received: 12 March 2014 / Accepted: 30 May 2014 / Published online: 11 June 2014

Abstract Densification and sintering of CeO_2 nanoparticles and their electrical properties were simultaneously studied as a function of temperature in controlled atmosphere using a modified dilatometer. CeO_2 nanoparticles simultaneously shrink and become more resistive upon initial heating, associated with desorption of water. The electrical conductance G at 300–550 °C revealed a pO_2 dependence described by $\log(G)=A+n\times\log(pO_2)$ with $n\sim-1/6$, consistent with n-type conduction. The results were analyzed with a defect equilibrium model based on the reduction of ceria and formation of doubly ionized oxygen vacancies and electrons. The activation energy was found equal to (1.3±0.1) eV, which results in an enthalpy of reduction of (2.7±0.4) eV, considerably lower than that for bulk ceria (~4.5 eV). The coarsening of particles during heat treatment at 800 °C were analysed assuming grain boundary diffusion-limited sintering. Although the coarsened powder shows a similar pO_2 dependence, the activation energy was considerably higher (1.9±0.1) eV, leading to a reduction enthalpy of (4.5±0.4) eV. The decrease in the enthalpy of reduction with decreasing particle size is consistent with the increasing fraction of oxide ions residing at the surface. Alternate interpretations based on space charge effects and surface adsorption/desorption were considered and found to be less consistent with the experimental results.

P. Knauth · J. Engel · S. R. Bishop · H. L. Tuller
Department of Materials Science and Engineering, Massachusetts Institute of Technology, Cambridge, MA 02139, USA

P. Knauth (✉)
Aix Marseille Université, CNRS, Madirel (UMR 7246), 13397 Marseille Cedex 20, France
e-mail: philippe.knauth@univ-amu.fr

S. R. Bishop
International Institute for Carbon Neutral Energy Research (WPI-I2CNER), Kyushu University, Nishi-ku, Fukuoka, Japan

Keywords Cerium dioxide · Ceria · Electronic conductivity · Defect chemistry · Electrical properties

1 Introduction

The intriguing properties of nanocrystalline metal oxides are generally associated with their high surface to volume ratio and high interface density [1–3]. Excellent performance has been reported in various energy storage and conversion applications: to give just a few examples, nanostructured oxide electrodes enable reduction of the operating temperature in solid oxide fuel cells [4]; significantly higher insertion capacity and better cycling have been demonstrated for nanostructured oxide electrodes in lithium-ion batteries [5, 6]; nanostructured electrodes improve the performance of dye-sensitized solar cells by several orders of magnitude compared to bulk electrodes [7, 8].

While the performance of nanomaterials is highly advantageous, the impact of the nanostructure on various physicochemical properties, including defect chemistry and electrical conductivity, remains poorly understood. Furthermore, given the large driving force for particle coarsening of nano-sized grains, it is essential to be able to predict how processing conditions are likely to impact properties. This is particularly true when considering how a change in particle size, during even medium temperature operation, may impact the lifetime and durability of electrodes or other device elements based on nanostructured oxides. A detailed characterization of the electrical properties of nanostructured powders as a function of particle size is of critical importance for (1) developing fundamental understanding of conduction mechanisms and defect chemistry in solids with high interface density; (2) detecting property variations due to coarsening of nanoparticles; and (3) tuning properties of nanomaterials prior to their

implementation and testing in devices, thereby saving time and improving the engineering process.

CeO_2 is a model material for such an investigation, given the many relevant defect and transport properties that have been reported for this oxide over the years. [9–16] Furthermore, nanocrystalline CeO_2 has many high added-value applications, including catalysis [17] and catalytic hydrogen production [18], oxygen storage [19, 20], energy conversion [4, 21] and gas sensors [22]; the particle size and shape are major parameters for tuning these properties and device performance. Many processing routes have been reported for fabricating nano-sized CeO_2 precursor powders with various shapes and sizes [23–26]. As a consequence, changes brought about by the nanostructure, and its evolution during thermal treatments at medium temperature and various oxygen partial pressures, can be systematically investigated.

In this work, the electrical properties, mechanical rearrangement and coarsening of CeO_2 nanoparticles during compaction and annealing at intermediate temperatures (300–550 °C) are simultaneously characterized using in-situ dilatometry and electrochemical impedance spectroscopy (EIS). The results are then discussed and analysed with the aid of densification, defect and transport models.

2 Experimental

High purity CeO_2 nanopowder (≈25 nm particle size, Sigma Aldrich) was purchased and used without further treatment. Powder X-Ray diffraction (XRD) was performed for phase analysis and average particle size determination [27] prior to and after heat treatment. A PANalytical X'Pert PRO X-ray diffractometer was used with Cu K α radiation (λ= 0.1504 nm) and 0.014 °/s scan rate.

The experimental arrangement, allowing simultaneous dilatometry and electrochemical impedance spectroscopy (EIS) measurements, was presented recently [28]. In short, the lightly compacted nanopowder of less than 1 mm thickness is contained in a quartz crucible with a thin sputtered Pt film at its base; a spring-loaded quartz rod retains the nanopowder, maintains the electrical contact to 3 mm diameter Pt electrodes sputtered on the quartz rod, and allows for the monitoring of the sample expansion or contraction. Other recent publications also describe the monitoring of the densification of a polycrystalline ceramic within a dilatometer by impedance spectroscopy [29, 30]. While outwardly similar to the arrangement described here, in the study by Muccillo and Muccillo, for example, there was no attempt to characterize the electrical properties of an ensemble of loose nanoparticles, but the study rather examined the impact of flash sintering on an yttria-stabilized zirconia (YSZ) ceramic that had been previously isostatically pressed at 210 MPa.

Mixtures of O_2/N_2 and $H_2/H_2O/N_2$ were used to fix the oxygen partial pressure (pO_2) within the sample chamber, with the pO_2 ranging from 1 to ~10^{-35} bar, measured by an in situ YSZ Nernst sensor or estimated using thermodynamic relationships. The gas ratios and flow rates were adjusted by mass flow controllers. EIS measurements were performed using a Novocontrol Alpha-A Impedance Analyzer (Hundsangen, Germany) over a frequency range of 0.1 Hz to 1 MHz and in a temperature range between 300 °C to 550 °C for nanocrystalline CeO_2 or up to 800 °C for microcrystalline CeO_2.

3 Results

3.1 Nanoparticle structure and size

The as-received nanopowders were found by powder XRD to solely contain the cubic fluorite CeO_2 phase (Fig. 1, black pattern). The relative Bragg peak intensities are very close to the JCPDS file values (blue lines in Fig. 1), showing the absence of predominant crystallite orientation. Using line profile analysis (Pseudo-Voigt) and the Scherrer equation, an average crystallite size of (26±2) nm was obtained, taking microstrain into account. Following an annealing treatment at 800 °C for 40 h (Fig. 1, red pattern), one notices a slight shift of the peak position vs. higher Bragg angles, indicating a decrease of the unit cell parameter; as the sample was treated at high pO_2 at the end of the experiment, this is consistent with a slightly higher oxygen deficiency of the as-received nanopowder. The average crystallite size after the experiment was (40±10) nm.

3.2 Compaction of CeO_2 nanopowders

Figure 2 shows a typical dilatometric curve obtained during the initial heating of the nanopowder. Rather than thermal

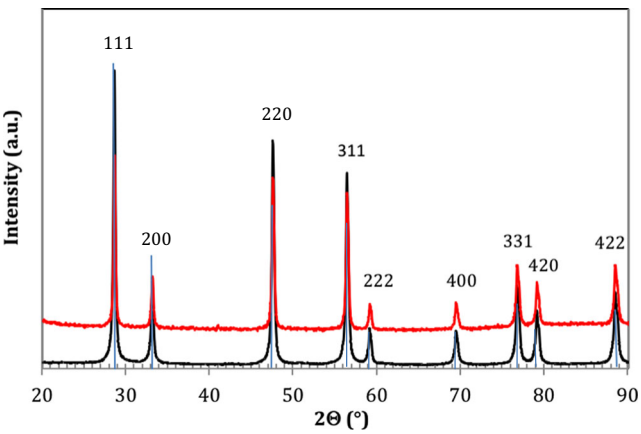

Fig. 1 XRD patterns of (**a**) as-received CeO_2 nanopowder (*black*) and (**b**) CeO_2 powder after experiment (*red*). The reference peaks of JCPDS file no. 00-004-0593 for CeO_2 are indicated by *vertical blue lines*

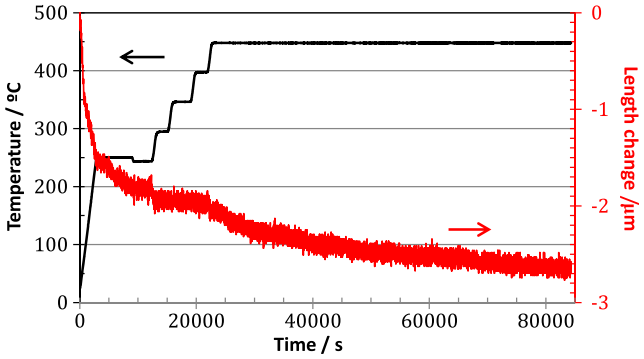

Fig. 2 Compaction of CeO_2 nanopowder during the first heating up to 450 °C at pO_2=0.2*bar* (*red line*). The *black line* represents the time-dependent temperature profile

expansion, an overall compaction by nearly 3 μm was observed upon heating up to 450 °C.

The compaction detected by dilatometry can be attributed to particle rearrangement into a denser structure and is also consistent with water loss. Slow particle coarsening of loose CeO_2 nanopowder was previously observed [18]. Repeated attempts to observe thermal or defect-induced dilation (i.e. chemical expansion [31]) by step changes of temperature or pO_2 and heating/cooling cycles were unsuccessful, given the higher observed level of compaction than that expected from thermal or chemical expansion of ceria.

3.3 Electrical properties of CeO_2 nanopowders

EIS measurements were performed as a function of temperature and pO_2 in order to identify the predominant conduction type. Upon initial heating, the electrical resistance increased; this is suspected to be due to progressive removal of water molecules and hydroxyl ions from the oxide surface. Adsorbed water is known to conduct protons on the surface of oxides [32–34] and water desorption upon heating results in a change in conduction mechanism from surface protonic to "bulk" transport, consistent with our prior study of nanocrystalline TiO_2 [28]. Following the 450 °C annealing shown in Fig. 2, electrical measurements during subsequent heating and cooling cycles were reproducible, although a small level of irreversible contraction continued to be observed for heat treatments above 400 °C, and were likely due to the rearrangements of particles during thermal cycling.

Figure 3(a) shows typical impedance spectra measured at pO_2=1 bar as a function of temperature and Fig. 3(b), impedance spectra measured at 550 °C as a function of pO_2. The spectra are characterized by nearly ideal semi-circles except for the lowest frequencies. The electrical properties were extracted from the spectra by fitting an equivalent circuit model, consisting of two parallel (resistor//constant phase element [CPE]) components in series, one representing the grain interior and the other partially blocking particle-particle

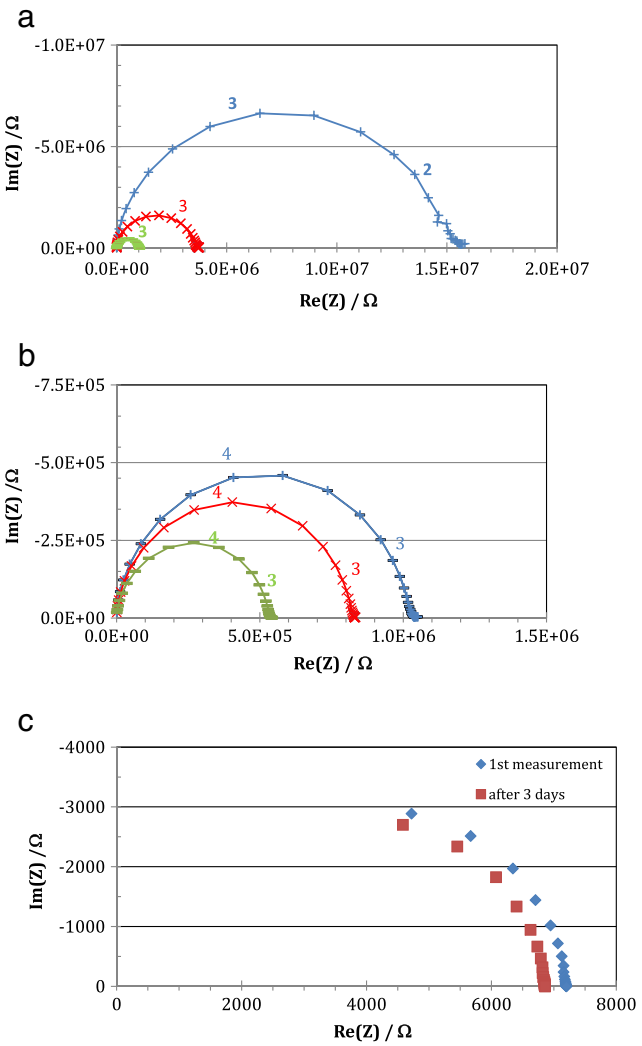

Fig. 3 (**a**) Complex impedance spectra (10^6–10^{-1} Hz) showing measured data points (*symbols*) and the result of equivalent circuit fitting (lines). The spectra were obtained for CeO_2 nanopowder under pO_2=1 bar at 450 °C (+), 500 °C (×), and 550 °C (−). Each numeric label is the logarithm (base 10) of frequency for the corresponding data point. (**b**) Complex impedance spectra (10^6–10^{-1} Hz) showing measured data points (*symbols*) and the result of equivalent circuit fitting (*lines*). The spectra were obtained for spherical CeO_2 nanopowder at 550 °C and various pO_2/*bar*: 0.05 (−), 0.1 (×), 1 (+). Each numeric label is the logarithm of frequency for the corresponding data point. (**c**). Variation of impedance spectra with time. The measurement conditions are 350 °C and $pO_2 \approx 10^{-38}$ *bar*

contacts. The impedance of a CPE can be expressed as $Z_{CPE}=(jY\omega)^{-n}$, where j is the imaginary unit, ω the angular frequency, Y the frequency-independent CPE constant and n the CPE exponent. n=1 describes an ideal capacitor with capacitance $Y=C$ [35]. Fig. 3(c) shows an example of the variation of the impedance spectra with time under conditions of 350 °C and $pO_2 \approx 10^{-38}$ bar. The fact that equilibration takes days at these temperatures suggests the importance of diffusion or surface oxygen exchange kinetics in controlling the overall redox kinetics.

The determined exponent for the high frequency response, n=(0.94±0.02), is independent of temperature and pO_2; the corresponding capacitance value, taken as the modulus of the CPE, has a weakly temperature-dependent value between 10 (300 °C) and 20 pF (550 °C). These parameters are consistent with a grain interior response, based on a bulk relative dielectric constant of approximately 25 [36] and a powder thickness of around 0.15 mm; at elevated temperatures, a dielectric constant on the order of 50 has been reported [37]. The small resistance associated with the low frequency tail on the main arc (most readily observed in Fig. 3(a) at 450 °C) can be attributed to partially blocking contacts between the loosely compacted powders. One should mention that similar bulk-like spectra have been obtained on dense nanocrystalline CeO_2, interpreted assuming parallel grain boundaries short-circuiting the bulk and modelled by application of a space charge model [12]. Kim and Maier pointed out that the bulk capacitance may still be observed, even if the conductance is determined by highly conducting space charge regions short-circuiting the grain interior [12].

The product of temperature and grain conductance is plotted in Fig. 4 as a function of reciprocal temperature; a double-logarithmic plot of grain conductance vs. oxygen partial pressure is shown in Fig. 5. The lack of data at intermediate pO_2 is typical for low to intermediate temperatures and is a consequence of the inability to achieve these pO_2s by either diluting oxygen gas with inert gases such as N_2 or by the application of buffer gas mixtures such as H_2/H_2O or CO/CO_2. The corresponding boundary conductance (low frequency) contribution is also displayed for comparison in the Arrhenius plot (Fig. 4). The conductance increases with increasing temperature for a given pO_2 (Fig. 4) and decreases with increasing pO_2 at constant temperature (Fig. 5); this is consistent with the

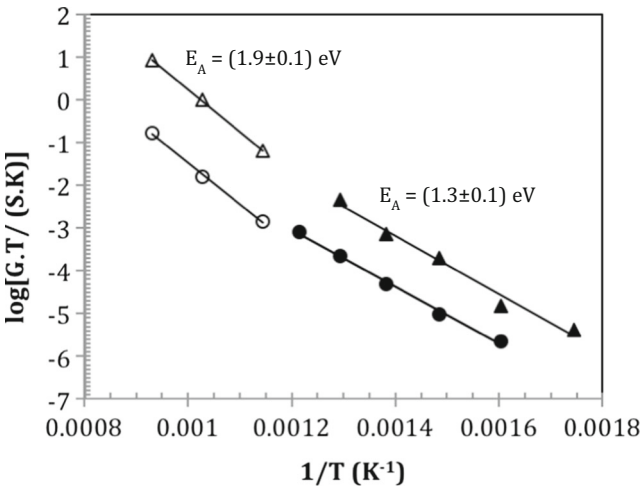

Fig. 4 Arrhenius-type representation of the electrical conductance G of compacted nominally undoped CeO_2 powders at pO_2=1 *bar*. *Full symbols*: nanosized powder, *open symbols*: powder after heating to 800 °C, *circles*: grain interior conductance, *triangles*: interface conductance

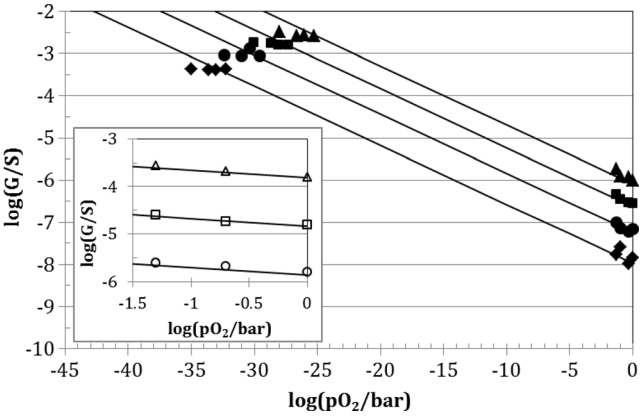

Fig. 5 Conductivity isotherms as function of pO_2 of CeO_2 nanopowder at 400 (*black diamond*), 450 (*black circle*), 500 (*black square*) and 550 °C (*black triangle*) and of coarsened CeO_2 powder (insert: 600 (*white circle*), 700 (*white square*) and 800 °C (*white triangle*)). The lines represent best fits to the data based on a $pO_2^{-1/6}$ dependence (Eq. 8)

behaviour of a large band-gap oxygen deficient n-type semiconductor (see discussion below).

For ionic conductors and small polaron semiconductors, the temperature dependence of conductivity can be described by Eq. 1:

$$In(\sigma T) = In(\sigma_0) - \frac{E_A}{kT} \quad (1)$$

Here, σ is the electrical conductivity, σ_0 the pre-exponential factor, E_A the activation energy of conduction, k Boltzmann's constant and T the absolute temperature. From Fig. 4, the activation energy for the nanopowders (slope at lower temperatures) amounts to (1.3±0.1) eV, in excellent agreement with the value reported in reference [12] and slightly higher than that for chemically processed *dense* nanocrystalline CeO_2 (1.16 eV [38, 39]) with smaller average grain size (10 nm). This is consistent with the increase of activation energy observed with increasing grain size in dense CeO_2 ceramics [38–40].

Linear fits to the isothermal double logarithmic plots in Fig. 5 reveal an overall approximate −1/6 power dependence at all temperatures. It can be observed that the conductance data at low pO_2 seem to plateau rather than maintain the logarithmic −1/6 power dependence. We return to this observation in the Discussion section below.

3.4 Sintering of CeO_2 nanoparticles and study of coarsened CeO_2

The sintering of nanoparticles was studied by heating the powder compacts to 800 °C. The dilatometric curve, showing normalized shrinkage vs. time, is presented in Fig. 6. Isothermal sintering has been described by Johnson [41], who showed that in bulk diffusion dominated sintering, a square root time dependence of the normalized shrinkage is observed,

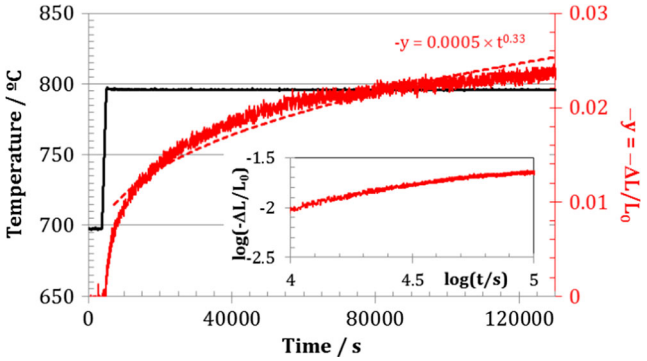

Fig. 6 Time dependence of normalized shrinkage -*y* (*red line*, see Eq. 2) of CeO_2 nanopowder at 800 °C and overlaid cubic root power law (*dotted red line*). The temperature change is shown in *black*. The equation in *red* is the best fit to the experimental data. Inset: double-logarithmic plot of normalized shrinkage vs. time

whereas grain boundary diffusion leads to a cubic root time dependence. Our data is best described by the latter relation (see the regression line and best-fit equation in Fig. 6).

$$y = \frac{\Delta L}{L_0} \approx \left(\frac{2.14\gamma\Omega b D_B}{kTa^4}\right)^{0.33} t^{0.33} \tag{2}$$

In this equation, y is the normalized shrinkage, γ the surface energy ($\gamma(CeO_2)$=1.2J/m^2 [42]), b the effective grain boundary width (taken as the classical Fisher value, 0.5 nm), and a the nanoparticle radius before sintering (taken as 12.5 nm). Ω is the volume of a cation vacancy, assessed from the radius of a Ce^{4+} cation (~0.12 nm [31]). Eq. 2 can be applied to estimate the grain boundary diffusion coefficient D_B in CeO_2, given that the sintering kinetics are limited by the slower cation diffusivity.

Based on the above model, we calculate a Ce grain boundary diffusion coefficient of ~10^{-18} cm^2/s. To the best of our knowledge, no other data have been published concerning the cation grain boundary diffusion coefficient in ceria. Only few literature values exist for comparison in other fluorite-type oxides: Kilo, for example, measured the temperature dependence of diffusion coefficients in yttria-stabilized zirconia by secondary ion mass spectrometry (SIMS) [43]. Using the reported equation, the grain boundary diffusion coefficient of Zr in YSZ at 1073 K, approximately 10^{-17} cm^2/s, is slightly higher than the value reported above, in line with the smaller radius of the Zr^{4+} ion [31].

Following the coarsening of the particles at 800 °C, the impedance spectra were measured at 600, 700 and 800 °C with the data obtained in artificial air reported in Fig. 7. Again, the spectra exhibit a semicircle characteristic of a resistor in parallel with a capacitor. Conductance values were extracted from best fits to these impedance data at various pO_2.

The temperature and oxygen partial pressure dependences of the conductance values obtained for coarsened CeO_2 are

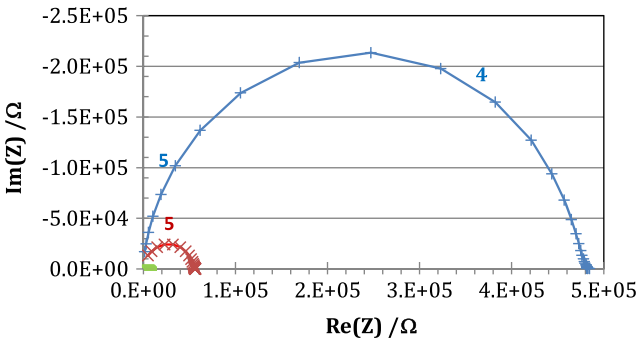

Fig. 7 Impedance spectra of coarsened CeO_2 powder compacts as function of temperature in dry air at 800 (−), 700 (×) and 600 °C (+)

reported in Figs. 4 and 5, together with the values obtained previously for the nanosized powder to allow a better comparison. From Fig. 4, an activation energy of (1.9±0.1) eV is determined by fitting Eq. (1) to the higher temperature data. Linear fits to the double logarithmic plots in Fig. 5 reveal an approximate −1/6 power dependence for coarsened, as for nanosized, CeO_2 powders.

The data for nanosized and coarsened CeO_2 are now discussed in terms of a defect equilibrium model.

4 Discussion

We now examine the data obtained in this study in terms of the defect relations presented below and the defect formation and mobility parameters reported in previous studies [15, 16, 38, 39]. Studies of the defect equilibria of CeO_2 were reported for single crystalline [15], microcrystalline [14], thin-film [44, 45] and nanocrystalline specimens [38, 39].

In order to interpret the temperature and pO_2 dependence of the measured electrical conductivity of the CeO_2 nanoparticles, it is instructive to first examine the accepted defect equilibrium model for bulk ceria. CeO_2 is well known to become oxygen deficient under reducing conditions at elevated temperatures by the formation of oxygen vacancies and electrons, described by:

$$O_O \rightleftarrows \frac{1}{2}O_2 + V_O^{\cdot\cdot} + 2e' \tag{3}$$

with the corresponding mass action relation given by

$$[V_O^{\cdot\cdot}]n^2 pO_2^{1/2} = K_R(T) = K_R^0 \exp\left(-\frac{\Delta_R H^0}{kT}\right) \tag{4}$$

in which $\Delta_R H°$ is the standard reduction enthalpy associated with reaction 3. Standard Kröger-Vink notation is used in which O_O, $V_O^{\cdot\cdot}$ and e' represent oxygen on a normal oxygen site, a doubly positively charged (relative to the normal lattice) oxygen vacancy and a negatively charged mobile electron,

respectively. The condition of charge neutrality can be approximated by:

$$2\left[V_O^{\cdot\cdot}\right] = n + A_{Ce}' \tag{5}$$

in which A_{Ce}' represent potential ionized acceptors, common inpurities in ceria.

Under highly reducing conditions (see Eq. 3), the electroneutrality condition is approximated by:

$$2\left[V_O^{\cdot\cdot}\right] \approx n \tag{6}$$

One can solve for the oxygen vacancy and electron concentrations under these conditions by substituting Eq. 6 into Eq. 4 to obtain:

$$2\left[V_O^{\cdot\cdot}\right] = n = (2K_R)^{1/3} pO_2^{-1/6} \tag{7}$$

This expression predicts that the electron and oxygen vacancy concentration are equal to each other within a factor of two. However, since electron mobilities are typically many orders of magnitude greater than that of ions, the electrical conductivity will largely be given by that of the electrons. For the case of ceria, the expression for the electronic conductivity is given by:

$$\sigma = ne\mu_e = \left(2K_R^0\right)^{1/3} e\mu_e^0 pO_2^{-1/6} \exp\left(-\frac{\Delta_R H^0/3 + E_{hop}}{kT}\right) \tag{8}$$

In this equation, e is the elementary charge, μ_e^0 the prefactor of small polaron mobility (which is thermally activated, E_{hop} being the hopping energy), with the other factors defined as above. The hopping energy in CeO_2 has been determined to be: E_{hop}=0.4 eV [15].

Often, particularly under oxidizing conditions, acceptor impurities dominate the right hand side of Eq. 5, leading to an approximate neutrality condition given by:

$$2\left[V_O^{\cdot\cdot}\right] \approx \left[A_{Ce}'\right] \tag{9}$$

Under these circumstances, n is given by:

$$n = \left(\frac{2K_R}{\left[A_{Ce}'\right]}\right)^{1/2} pO_2^{-1/4} \tag{10}$$

In this high pO_2 regime, the ionic conductivity is predicted to be pO_2 independent, as is the case for heavily acceptor doped ceria, while the electronic conductivity, which becomes predominant under more reducing conditions, follows the predicted $pO_2^{-1/4}$ dependence. Since the experimental results obtained in this study show the conductance to largely follow a $pO_2^{-1/6}$ dependence (see Fig. 5), we consider Eq. 8 when attempting to extract the relevant defect formation enthalpy. Additionally, it has been suggested that p-type conductivity exists for ceria in high pO_2, though in the present case there is no characteristic plateau or increase in conductivity with pO_2 [46, 47]. We do note an apparent weakening of the pO_2 dependence of the conductivity under highly reducing conditions, particularly for the two lowest pO_2 at each isotherm. This may be related to the onset of the well-known maximum conductivity exhibited by ceria under highly reducing conditions brought on by defect interactions at large deviations from stoichiometry [16, 48]. Alternatively, it may reflect difficulty in attaining gas phase equilibrium between H_2 and H_2O at the highest H_2/H_2O ratios at these temperatures. The O_2 partial pressures were calculated assuming thermodynamic equilibrium between H_2 and H_2O. The consistency of the calculated values at 550 °C were checked against the readings of a Nernst-type oxygen sensor and found in good agreement. The use of Pt sample electrodes is a key factor in overcoming kinetic barriers to the establishment of gas phase equilibrium between H_2 and H_2O. Nevertheless, the achievement of equilibration at the most extreme reducing conditions, and at low temperatures, may be suspect [48].

From the temperature dependence of the electrical conductivity of the ceria nanoparticles within the $pO_2^{-1/6}$ regime, assuming a negligible temperature and pO_2 dependence of the hopping energy as well as negligible space charge effects (see below), one can extract the enthalpy of reduction from Eq. 8. Given the measured activation energies of (1.3±0.1) eV for the nanopowders prior to coarsening and of (1.9±0.1) eV post coarsening, as reported above, one obtains $\Delta_{red}H°$=(2.7 ±0.4) eV for the nanopowder and $\Delta_{red}H°$=(4.5±0.4) eV for the coarsened CeO_2, nearly double that of the nanopowder. These values are in good agreement with data reported for nominally undoped nanocrystalline ceria (2.3 eV [38, 39]) and single crystalline ceria (4.7 eV [16]). Given that smaller particles have a higher surface to volume ratio, there is a larger fraction of oxide ions residing near the surface in nanocrystalline as compared to microcrystalline oxides. Therefore, the lower standard enthalpy of reduction derived for such nanoparticles is consistent with the considerably lower energy calculated for the removal of oxygen from the surface of ceria as compared to that in the bulk [49–51]. Similar findings have been reported in the case of dense nanocrystalline TiO_2 [13, 28, 52]. In the following, space charge and gas adsorption effects are considered, but found to be less consistent with the above interpretation of thermodynamic behavior.

Earlier studies, based on coulometric titration [53] and thermogravimetry coupled with mass spectroscopy [54], have reported oxygen nonstoichiometry data for ceria nanoparticles. In the coulometric titration study by Porat et al. [53], the oxygen nonstoichiometry δ (in $CeO_{2-\delta}$) followed a dependence given by

$$\delta = K_r^0 exp\left(-\frac{0.36eV}{kT}\right) pO_2^{-1/2} \tag{11}$$

which, considering the much steeper pO_2 dependence than observed for the electrical conductivity ($pO_2^{-1/6}$), cannot correspond to δ derived from the generation of doubly ionized vacancies as required by Eq. 7. Two possible interpretations were offered by Porat et.al. In one model, nonstoichiometry in these 10 nm size particles is assumed to be dominated by the generation of uncharged oxygen vacancies, i.e.

$$O_O \rightarrow V_O + 1/2O_2 \tag{12}$$

with the corresponding mass action relation

$$[V_O]pO_2^{1/2} = K_r(T) \tag{13}$$

leading to:

$$[V_O] = \delta = K_r(T)pO_2^{-1/2} \tag{14}$$

A provided alternative explanation attributes the reversible loss and gain of oxygen to Langmuir surface adsorption, described by

$$O_2 + 2V_{ad} \Leftrightarrow 2O_{ad} \tag{15}$$

where V_{ad} and O_{ad} correspond to empty and occupied surface adsorption sites, respectively, along with the following mass action relation

$$\theta \Big/ (1-\theta) = K_{ad}^{1/2} pO_2^{1/2} \tag{16}$$

where θ is the fraction of occupied adsorption sites. At high pO_2, θ approaches unity and so

$$(1-\theta) = \delta \cong K_{ad}^{-1/2} pO_2^{-1/2} \tag{17}$$

which also satisfies the dependence reported in Eq. 11.

Kim et al., examined oxygen nonstoichiometry in two variants of chemical derived ceria nanoparticles of 12 nm in diameter by thermogravimetry (TG) and mass spectroscopy (MS) [54]. Total weight changes in the specimens were dominated by water desorption/adsorption and so the amount of oxygen released or taken up was calculated from an analysis of the mass spectroscopic oxygen signal change induced by stepwise temperature variations. The authors concluded that the surface is predominantly responsible for the measured change in δ. The two sets of specimens exhibit a weaker dependence of log δ on log pO_2 of −0.28±0.02 and −0.11 than Porat et al.'s coulometric titration data (slope of~−0.5). The respective activation energies of 0.4 and 0.2 eV, however, bracket the value of 0.36 eV reported by coulometric titration. Kim et al. attribute their observed data to space charge effects, assuming a net positive surface charge due to the segregation of donor impurities to the surface. No attempt was made to derive the space charge potential from the measured activation energies of 0.4 and 0.2 eV nor to explain the source of donor impurities.

Both the titration and TGA/MS studies were limited to relatively high pO_2, 10^{-5} to 0.21 atm and 10^{-4} to 0.21 atm, respectively, and at least in the report by Kim et al. were heavily impacted by water desorption/adsorption. In the present study, pretreatment assured that surface water no longer dominated the transport properties of the ceria nanoparticles. Furthermore, the pO_2 range was much more extensive, extending from 1 atm down to as low as 10^{-35} atm (Fig. 5). As pointed out above, aside from the somewhat scattered data at the very lowest pO_2, the conductivity data fit well overall, over an extremely wide pO_2 range, to a $pO_2^{-1/6}$ dependence. Lee et al. [44] in a recent analysis of the pO_2 dependence of ceria thin films, also over a very wide pO_2 range, attributed an enhanced electronic conductivity, as compared to microcrystalline ceria, at high pO_2 to a space charge model, but found a transition to bulk control at low pO_2. This transition was attributed to a systematic shrinkage of the space charge width, ultimately to below 1 nm, with increasing carrier concentration. The fact that in the present case there is no corresponding change in the conductivity pO_2 dependence with changing pO_2 suggests that space charge effects are not significantly impacting the electron density, even at high pO_2.

Finally, one may also question if the measured impedance truly corresponds to the 'bulk' properties of the nanoparticles and does not represent surface adsorption/desorption effects as reported for semiconducting metal oxide sensor materials, such as SnO_2. However, the equilibration times of the order of days (see Fig. 3(c)) following a change in pO_2 support diffusion and/or surface exchange-limited kinetics as responsible for the redox kinetics. Furthermore, the interpretation that this change in resistance is due to a change in the oxygen stoichiometry of the CeO_2 particles is supported by the fact that the resistance values are consistent with different buffer gas mixtures (O_2/N_2 and $H_2O/H_2/N_2$) used to set pO_2. Very different values of resistance would be expected if gas chemisorption was taking place, which is normally highly dependent on the nature of the gas molecules [55, 56]. Furthermore, no sensitivity maximum as a function of temperature was observed, a typical feature of sensors operating on the basis of a chemisorption process.

5 Conclusions

Nanopowders are rarely electrically characterized before being integrated into a device despite the importance of their electrical properties. In this study, the compaction and sintering of ceria nanopowders was studied in-situ using combined dilatometry/impedance spectroscopy. A full heating cycle is required to reach reproducible electrical resistance values at a given temperature and pO_2, eliminating spurious

effects related to adsorbed water. The time-dependent normalized shrinkage of the ceria nanopowder, achieved by heating to 800 °C, could be described by a grain-boundary limited sintering process with the grain boundary diffusion coefficient of cerium cations deduced to be ~10^{-18} cm^2/s. While the electrical conductivity of both the nanopowders and the coarsened ceria exhibited the same $pO_2^{-1/6}$ dependence, the activation energy characterizing the electrical conductivity of the nanopowders was found to be distinctly lower from that of coarsened ceria (1.3±0.1 vs 1.9±0.1 eV). Oxygen loss was found to be well described by defect equilibria governed by the generation of doubly charged oxygen ion vacancies and excess electrons, with the enthalpy of reduction found to decrease from $\Delta_{red}H°$=(4.5±0.4) eV for the coarsened CeO_2 to $\Delta_{red}H°$=(2.7±0.4) eV for the nanopowder. The decrease in the enthalpy of reduction with decreasing particle size is consistent with the increasing fraction of oxide ions residing near the surface that are calculated to be much more easily removed than oxygen residing within the interior of the particle. Alternate interpretations based on space charge and surface adsorption/desorption phenomena were considered and found to be less consistent with the experimental results.

Acknowledgments The authors acknowledge the US-Department of Energy—Basic Energy Sciences, Grant No. DE-SC0002633 for financial support. This work made use of the MRSEC Shared Experimental Facilities at MIT, supported by the National Science Foundation under award number DMR-0819762. P. K. wishes to thank H. L. T. for the kind hospitality during his sabbatical at the Massachusetts Institute of Technology. The authors thank Dr. Scott Speakman for assistance with the XRD analysis. SRB thanks I2CNER, supported by the World Premier International Research Initiative (WPI), MEXT Japan, for travel funding.

References

1. H.L. Tuller, Solid State Ionics **131**, 143 (1998)
2. H.L. Tuller, S.J. Litzelman, W. Jung, Phys. Chem. Chem. Phys. **11**, 3023 (2009)
3. J. Maier, in *Nanocrystalline Metals and Oxides—Selected Properties and Applications*, ed. by P. Knauth, J. Schoonman (Kluwer, Boston, 2002), p. 84
4. E.D. Wachsman, K.T. Lee, Science **334**, 935 (2011)
5. T. Djenizian, I. Hanzu, P. Knauth, J. Mater. Chem. **21**, 9925 (2011)
6. A.S. Arico, P. Bruce, B. Scrosati, J.M. Tarascon, W. Van Schalkwijk, Nat. Mater. **4**, 366 (2005)
7. G.K. Mor, O.K. Varghese, M. Paulose, K. Shankar, C.A. Grimes, Sol. Energy Mater. Sol. Cells **90**, 2011 (2006)
8. A. Hagfeldt, M. Gratzel, Chem. Rev. **95**, 49 (1995)
9. M. Mogensen, N.M. Sammes, G.A. Tompsett, Solid State Ionics **129**, 63 (2000)
10. J.H. Hwang, D.S. McLachlan, T.O. Mason, J. Electroceram. **3**, 7 (1999)
11. J.H. Hwang, T.O. Mason, Z. Phys. Chem. **207**, 21 (1998)
12. S. Kim, J. Maier, J. Electrochem. Soc. **149**, J73 (2002)
13. P. Knauth, H.L. Tuller, Solid State Ionics **136**, 1215 (2000)
14. H.L. Tuller, A.S. Nowick, J. Electrochem. Soc. **122**, 255 (1975)
15. H.L. Tuller, A.S. Nowick, J. Phys. Chem. Solids **38**, 859 (1977)
16. H.L. Tuller, A.S. Nowick, J. Electrochem. Soc. **126**, 209 (1979)
17. A. Tschope, J.Y. Ying, H.L. Tuller, Sensors Actuators B-Chem. **31**, 111 (1996)
18. B. Neltner, B. Peddie, A. Xu, W. Doenlen, K. Durand, D.S. Yun, S. Speakman, A. Peterson, A. Belcher, ACS Nano **4**, 3227 (2010)
19. P. Knauth, H.L. Tuller, J. Eur. Ceram. Soc. **19**, 831 (1999)
20. M. Kuhn, S.R. Bishop, J.L.M. Rupp, H.L. Tuller, Acta Mater. **61**, 4277 (2013)
21. J.L.M. Rupp, A. Infortuna, L.J. Gauckler, Acta Mater. **54**, 1721 (2006)
22. J.L.M. Rupp, L.J. Gauckler, Solid State Ionics **177**, 2513 (2006)
23. S.W. Yang, L. Gao, J. Am. Chem. Soc. **128**, 9330 (2006)
24. H.X. Mai, L.D. Sun, Y.W. Zhang, R. Si, W. Feng, H.P. Zhang, H.C. Liu, C.H. Yan, J. Phys. Chem. B **109**, 24380 (2005)
25. C.W. Sun, H. Li, L.Q. Chen, Energy Environ. Sci. **5**, 8475 (2012)
26. C. Laberty-Robert, J.W. Long, E.M. Lucas, K.A. Pettigrew, R.M. Stroud, M.S. Doescher, D.R. Rolison, Chem. Mater. **18** (2006)
27. A. Weibel, R. Bouchet, F. Boulc'h, P. Knauth, Chem. Mater. **17**, 2378 (2005)
28. Johanna Engel, Sean R. Bishop, Harry L. Tuller, L. Vayssieres, in *Advanced Functional Materials*, (2014). doi:10.1002/adfm.201400203
29. R. Muccillo, E.N.S. Muccillo, J. Eur. Ceram. Soc. **33**, 515 (2013)
30. O. Mazar, in *PhD thesis*, Technion, Israel Institute of Technology, Haifa, Israel (2013)
31. D. Marrocchelli, S.R. Bishop, H.L. Tuller, B. Yildiz, Adv. Funct. Mater. **22**, 1958 (2012)
32. H.J. Avila-Paredes, E. Barrera-Calva, H.U. Anderson, R.A. De Souza, M. Martin, Z.A. Munir, S. Kim, J. Mater. Chem. **20**, 6235 (2010)
33. F. Maglia, I.G. Tredici, G. Spinolo, U. Anselmi-Tamburini, J. Mater. Res. **27**, 1975 (2012)
34. Y. Nigara, K. Kawamura, T. Kawada, J. Mizusaki, M. Ishigame, J. Electrochem. Soc. **146**, 2948 (1999)
35. J.R. MacDonald, *Impedance Spectroscopy: Emphasizing Solid Materials and Systems*, (Wiley, 1987)
36. A.S. Nowick, A.V. Vaysleyb, I. Kuskovshy, Phys. Rev. B **58**, 8398 (1998)
37. N.H. Perry, T.C. Yeh, T.O. Mason, J. Am. Ceram. Soc. **94**, 508 (2011)
38. Y.M. Chiang, E.B. Lavik, I. Kosacki, H.L. Tuller, J.Y. Ying, Appl. Phys. Lett. **69**, 185 (1996)
39. Y.M. Chiang, E.B. Lavik, I. Kosacki, H.L. Tuller, J.Y. Ying, J. Electroceram. **1**, 7 (1997)
40. A. Tschöpe, Solid State Ionics **139**, 267 (2001)
41. D.L. Johnson, J. Appl. Phys. **40**, 192 (1969)
42. S. Hayun, S.V. Ushakov, A. Navrotsky, J. Am. Ceram. Soc. **94**, 3679 (2011)
43. S. Swaroop, M. Kilo, C. Argirusis, G. Borchardt, A.H. Chokshi, Acta Mater. **53**, 4975 (2005)
44. K.R. Lee, J.H. Lee, H.I. Yoo, Phys. Chem. Chem. Phys. **15**, 15632 (2013)
45. S.J. Litzelman, H.L. Tuller, Solid State Ionics **180**, 1190 (2009)
46. Y.P. Xiong, H. Kishimoto, K. Yamaji, M. Yoshinaga, T. Horita, M.E. Brito, H. Yokokawa, Solid State Ionics **192**, 476 (2011)
47. H. Yahiro, Y. Eguchi, K. Eguchi, H. Arai, J. Appl. Electrochem. **18**, 527 (1988)
48. S.R. Bishop, K.L. Duncan, E.D. Wachsman, Electrochim. Acta **54**, 1436 (2009)
49. T.X.T. Sayle, S.C. Parker, C.R.A. Catlow, J. Chem. Soc. Chem. Comm. 977 (1992)
50. W.C. Chueh, A.H. McDaniel, M.E. Grass, Y. Hao, N. Jabeen, Z. Liu, S.M. Haile, K.F. McCarty, H. Bluhm, F. El Gabaly, Chem. Mater. **24**, 1876 (2012)
51. S.R. Bishop, K.L. Duncan, E.D. Wachsman, Acta Mater. **57**, 3596 (2009)
52. P. Knauth, H.L. Tuller, J. Appl. Phys. **85**, 897 (1999)

53. O. Porat, E.B. Lavik, H.L. Tuller, Y.-M. Chiang, in *Nanophase and Nanocomposite Materials II*, ed. by S. Komarneni, J. Parker, H. Wollenberger (Materials Research Society, Pittsburgh, 1997), p. 99
54. S. Kim, R. Merkle, J. Maier, Surf. Sci. **549**, 196 (2004)
55. O.K. Varghese, L.K. Malhotra, J. Appl. Phys. **87**, 7457 (2000)
56. W. Gopel, K.D. Schierbaum, Sensors Actuators B-Chem. **26**, 1 (1995)